

A Resource Efficient Quantum Kernel

Utkarsh Singh,^{1,2} Jean-Frédéric Laprade,³ Aaron Z. Goldberg,¹ and Khabat Heshami^{1,2,4}

¹*National Research Council of Canada, 100 Sussex Drive, Ottawa, Ontario K1N 5A2, Canada*

²*Department of Physics, University of Ottawa, 25 Templeton Street, Ottawa, Ontario, K1N 6N5 Canada*

³*Institut quantique, Université de Sherbrooke Sherbrooke, QC J1K 2R1, Canada*

⁴*Institute for Quantum Science and Technology, Department of Physics and Astronomy, University of Calgary, Alberta T2N 1N4, Canada*

Quantum processors may enhance machine learning by mapping high-dimensional data onto quantum systems for processing. Conventional quantum kernels, or feature maps, for encoding data features onto a quantum circuit are currently impractical, as the number of entangling gates scales quadratically with the dimension of the dataset and the number of qubits. In this work, we introduce a quantum kernel designed to handle high-dimensional data with a significantly reduced number of qubits and entangling operations. Our approach preserves essential data characteristics while promoting computational efficiency, as evidenced by extensive experiments on benchmark datasets that demonstrate a marked improvement in both accuracy and resource utilization, as compared to state-of-the-art quantum feature maps. Our noisy simulations results combined with lower resource requirements highlight our kernel's ability to function within the constraints of noisy intermediate-scale quantum devices. Through numerical simulations and small-scale implementation on a superconducting circuit quantum computing platform, we demonstrate that our scheme performs on par or better than a set of classical algorithms for classification. Our findings herald a promising avenue for the practical implementation of quantum machine learning algorithms on near future quantum computing platforms.

I. INTRODUCTION

High-dimensional data is prevalent in modern machine learning tasks, including image and speech recognition, natural language processing, and medical diagnostics. While classical machine learning techniques can handle these high-dimensional problems, they often require substantial computational resources, particularly as the dimensionality of the data increases [1–3]. Quantum computing has emerged as a promising avenue to address these challenges. Quantum kernel methods, for instance, have shown potential for accelerating data analysis by efficiently learning relationships in high-dimensional spaces encoded into quantum states [4–9]. To harness large-dimensional Hilbert spaces for processing data, quantum computers need to efficiently encode classical data onto quantum states. These quantum feature maps are required for quantum support vector classification [10–14] and quantum neural networks [10, 11, 14–16], including data reuploading [17], and are germane to essentially all quantum machine learning paradigms. Yet, the most popular feature maps require numbers of qubits and controlled-not (CNOT) gates linear or quadratic in the number of data features, respectively, severely curtailing their practical application. We introduce a feature map whose qubit requirement is reduced by a factor of at least two and whose CNOT-gate requirement is reduced to linear in the number of qubits and show these

improvements to be sufficient for practical application on current devices.

Quantum feature maps [18] translate classical data into a quantum form that can be manipulated using quantum circuits, enabling the application of quantum algorithms [11]. The qubit and entangling gate requirements for conventional feature maps pose a significant limitation for practical applications, particularly in era of noisy intermediate-scale quantum (NISQ) devices, where the number of qubits is limited and gate errors are prohibitively large [19]. The development of efficient quantum feature maps that can effectively encode high-dimensional classical data onto quantum states while minimizing the number of qubits remains an active area of research, with several proposed embedding schemes under exploration [4, 9, 20].

Here, after introducing our quantum feature map with the reduced resource requirements, we examine its performance using a kernel method in classification of various datasets. We compare our results with several classical methods and the commonly used Pauli feature map known as the ZZ feature map and consistently show competing performance. We present a detailed background of quantum feature maps and their challenges in Section I A. In Section II A we introduce our approach. We lay out our experimental methodology and results in Section II B, including small-scale tests on IBM's ibm_quebec machine. Our results stimulate considerations of quantum machine learning as an early practical application of application-starved NISQ

devices. It is important to note that in our work, we utilize this feature map within a predefined quantum kernel function for the support vector classifier (SVC) algorithm in Qiskit [14, 21]. As a result, we will refer to both the feature map and the kernel as CPMMap.

A. Feature Maps

Quantum feature maps (QFMs) play a pivotal role in quantum machine learning, enabling the encoding of classical data into the quantum state space. This encoding process transforms classical vectors into the amplitudes of quantum states, thus facilitating quantum processing. In this section, we delve into the mathematical foundations of QFMs and explore their applications and limitations.

1. Mathematical Definition

A quantum feature map is defined as a function $\Phi : \mathbb{R}^n \rightarrow \mathcal{H}$, where \mathcal{H} is the Hilbert space of a quantum system. Given a classical vector $\mathbf{x} \in \mathbb{R}^n$, the map Φ transforms \mathbf{x} into a quantum state:

$$\Phi(\mathbf{x}) = U_\Phi(\mathbf{x})|0\rangle = \sum_{i=0}^{2^n-1} f_i(\mathbf{x})|i\rangle, \quad (1)$$

where $f_i(\mathbf{x})$ are QFM-dependent functions of the classical data and $\{|i\rangle\}$ represents the orthonormal set of computational basis states. The most common class of feature maps comprises the Pauli feature maps.

2. Pauli Feature Maps

The Pauli Feature Map encodes classical data into the state space of a quantum system. It is formalized as

$$U_\Phi(\mathbf{x}) = \exp \left(i \sum_{S \subseteq T} \phi_S(\mathbf{x}) \prod_{i \in S} P_i \right) H^{\otimes n}, \quad (2)$$

where S indexes subsets of qubits, T encompasses all such subsets, and each P_i represents one of the Pauli matrices $\{I, X, Y, Z\}$ acting on the qubit labeled by i . The factor $H^{\otimes n}$ applies a Hadamard gate H on each of the n qubits to transform computational basis states into superpositions thereof. The function ϕ_S is defined as the data-mapping function, with $\phi_S(\mathbf{x}) = x_i$ when

S is a singleton and $\phi_S(\mathbf{x}) = \prod_{j \in S} (\pi - x_j)$ otherwise, thus capturing both individual feature impacts and the impacts of higher-order interactions between features within the quantum state [4, 22]; in this sense the scalar functions $\phi(\mathbf{x})$ are components of the mapping function Φ .

Among the commonly used Pauli feature maps is the *Pauli-Z Feature Map* (also referred to as the ZFeatureMap), where each subset S is a singleton and each P_i corresponds to a Pauli-Z operation. This map encodes classical data by applying phase shifts relative to each data feature x_i , such that each qubit in the circuit experiences a phase rotation as dictated by the respective feature value. The corresponding transformation is expressed as

$$U_\Phi(\mathbf{x}) = \bigotimes_i e^{-ix_i Z} H, \quad (3)$$

where the tensor product runs over all qubits. The result is a quantum state separable between all qubits where for each qubit a data feature is encoded in the relative phase between computational basis states [4, 14].

A second widely adopted feature map is the *Pauli-ZZ Feature Map* (ZZFeatureMap), which extends the Pauli-Z map by incorporating interactions between qubits. This is achieved through alternating single-qubit Z-rotations and two-qubit ZZ-entangling gates. The latter take the form

$$U_\Phi(\mathbf{x}) = \exp \left(i \sum_{\{i,j\} \in T} \phi_{\{i,j\}}(\mathbf{x}) Z_i Z_j \right) H^{\otimes n} \quad (4)$$

and enable the map to encode both individual contributions and pairwise interactions between features into an entangled quantum state. Owing to its capacity to enrich the expressivity of the quantum feature space, the ZZFeatureMap is one of the most commonly used data encoding methods in quantum classification tasks [4, 22–25].

3. Challenges and Limitations

All of the aforementioned quantum feature maps require the number of qubits to grow linearly with the dimensionality of the data, requiring one qubit per datum. This requirement becomes prohibitive with high-dimensional data, particularly with current NISQ devices [19]. The ZZFeatureMap tends to perform better than the ZFeatureMap so, for this study, we will only

consider the ZZFeatureMap. In the case of ZZFeatureMap, the circuit depth grows linearly and the number of CNOT gates in the circuit grows quadratically with the number of features in the data; this will later be seen in Fig. 2. Appendix B explains why we choose the ZZFeatureMap over the ZFeatureMap for our comparisons, as the latter can seldom be used on its own when nonlinear functions of the input data are necessary. Our feature map has better resource costs than the ZZFeatureMap while still performing well, which is crucial for comparison because one can always find feature maps that are less resource intensive but with inferior performance.

II. RESULTS

A. CPMMap

Our proposed CPMMap gets its inspiration from quantum convolutional neural networks [15]. The key features of the latter, like classical convolutional neural networks, are convolutional layers that find crucial features in data and pooling layers that aggregate several of these features in to a smaller number (often one) in order to reduce the total number of features. The CPMMap has a number of layers that first find crucial features in data and then aggregate several features into a smaller number in order to reduce the total number of features. Since it is quantum, all of the operations are performed on qubits using unitary gates and serve to focus the data's features onto a reduced number of qubits, such that the resources made available by the aggregation can be used for further processing.

1. Quantum Convolutional Neural Network

Quantum convolutional neural networks (QCNNs) are a quantum analog of classical convolutional neural networks (CNNs), designed to process quantum data and perform quantum computations. In a QCNN, the convolutional layer applies a series of quantum gates (U_1 and U_2) to small, localized regions of the input quantum data, which are parameterized by a set of learnable parameters. These quantum gates can be thought of as the quantum equivalent of the convolutional filters in classical CNNs. They are designed to detect various features or patterns in the input data, such as edges or textures in an image. The parameters of these quantum gates are updated during the training

process using quantum versions of classical optimization techniques, such as gradient descent. This allows the QCNN to learn to detect features that are relevant for a particular task, such as classifying images or detecting anomalies in a dataset [15].

The pooling layers in a QCNN are responsible for reducing the dimensionality of the quantum data, thereby reducing the computational cost of subsequent layers and helping to make the network invariant to small translations in the input. In a quantum pooling layer (V_i and \mathcal{M}), a subset of the qubits is measured, and the outcomes of these measurements are used to decide which qubits to keep and which to discard. This is analogous to the way classical pooling layers (e.g., max-pooling layers) retain only the most important information from the input, discarding the rest to produce a condensed representation. The pooling operation in QCNNs is non-trivial due to the inherent nature of quantum measurements, which are probabilistic and cause the quantum state to collapse. Designing effective quantum pooling operations that preserve relevant information while reducing dimensionality is an active area of research [15, 16]. An example of a QCNN with 8 qubits is featured in Fig. 1(d), where the measurement and feedforward operations are seen to halve the number of remaining qubits at each step.

2. QCNN to CPMMap

The CPMMap uses an idea reminiscent of the QCNN to encode more features in a limited space. Instead of discarding the qubits after the pooling layer, the CPMMap uses those leftover qubits for processing more features; pooling is thus replaced by partitioning. However, since it is a kernel, we do not perform any optimization on the parameters, and measurement happens only at the end, if at all; the new data are uploaded in a coherent process and all of the encoded data can be processed in a multitudine of ways prior to measurement. Therefore, it resembles a QCNN structurally, but its working is different. The CPMMap uses two circuits similar to the convolutional and pooling circuits of a QCNN: the unitaries C inspired by the convolutional layers (U_1 and U_2) and the unitaries P inspired by the pooling layers (V_1 and \mathcal{M} and V_2 and \mathcal{M}), which do not require subscripts because they are the same at each layer of the network. These together pool down the information, for example, from n qubits to $n/2$ qubits in each layer; then, the process is repeated iteratively on the remaining $n/2$ qubits. n qubits can thus house approximately $n + \frac{n}{2} + \frac{n}{4} + \dots = 2n$ features, with the total

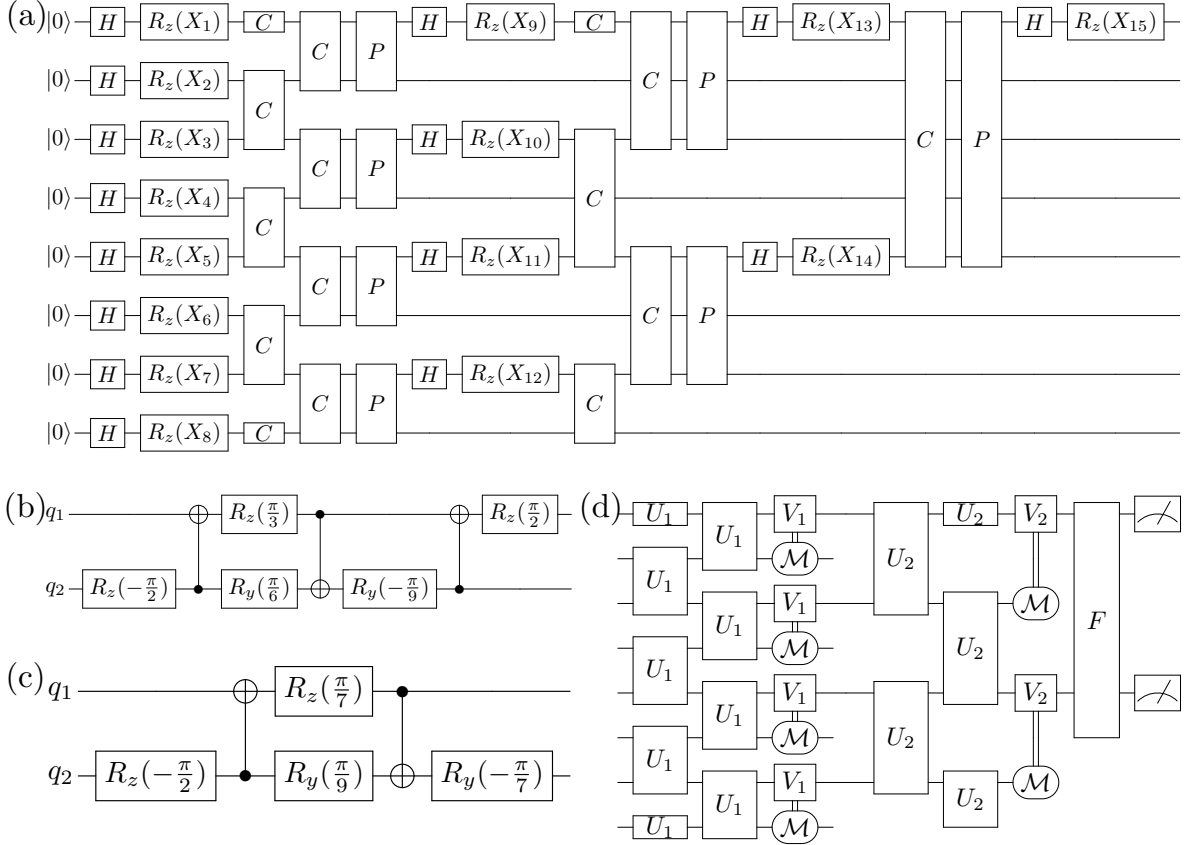


FIG. 1. (a) A CPMap with 8 qubits encoding 15 features. The qubits are then output to be used coherently in any application (including measurement, repetition of the kernel, and input to a quantum neural network). H is the Hadamard gate and $R_z(X_i)$ is a single-qubit rotation around the z axis by angle X_i . (b) Diagram of the C unitary. (c) Diagram of the P unitary. (d) An illustration of a quantum CNN with 8 qubits. The two-qubit unitaries U_1 and U_2 perform convolutions, then the pooling operations are done by measurements \mathcal{M} on one qubit followed by feedforward unitaries V_1 and V_2 on the other qubit; all such operations involve parameters that must be trained. While (d) uses pooling operations, (a) adopts a similar architectural flow but replaces them with the unitary P , allowing more data features to be encoded before the subsequent layer.

number of qubits required to encode N features being exactly given by the meta-Fibonacci sequence for $s=0$ [26, 27]. This sequence is given by

$$a(N) = a(N-a(N-1)) + a(N-1-a(N-2)), \quad (5)$$

where $a(1) = a(2) = 1$.

An exemplary diagram of a CPMap and a QCNN can be found in the Fig. 1. The example is based on the QCNN from Ref. [15]. Individual features are encoded in the standard way by the application of the Pauli-Z map and any similar encoding can be used. The measurement and feedforward part of the circuit in (d) is replaced with the unitary P in (a). If we instead con-

sider pooling unitaries that each focus the data from n qubits onto a number of qubits smaller than $n/2$ (such as n/m) the same strategy can be used to encode even more data points onto the same fixed number of qubits (nm) because greater than $n/2$ qubits ($n\frac{m-1}{m}$) remain for the subsequent iteration. These allow for practically useful increases in the number of features that can be processed by machines with limited numbers of qubits.

With this general structure in mind, one can specify different choices of the convolutional unitaries C and the pooling unitaries P . We can choose how many qubits each acts on, but we must then assess whether a given choice succeeds for a given machine learning task and also assess the total complexity of the circuit

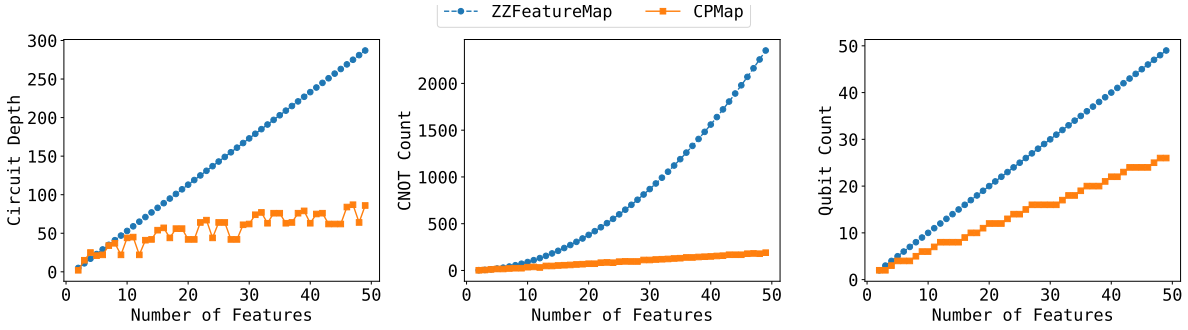


FIG. 2. CPMMap vs. ZZfeatureMap based on quantum resources. (a) Circuit depth vs. number of features (b) Number of CNOTs used in the circuit vs. number of features (c) Number of qubits required vs. number of features for both of the features maps for different number of features in the dataset

required to implement these unitaries. To keep things simple, we focus on two-qubit unitaries and represent them in a form inspired by the fact that we can write any matrix in $U(4)$ in the form [14, 28]:

$$U = (A_1 \otimes A_2)N(\alpha, \beta, \gamma)(A_3 \otimes A_4), \quad (6)$$

where $A_i \in \text{SU}(2)$ and $N(\alpha, \beta, \gamma) = \exp[i(\alpha X \otimes X + \beta Y \otimes Y + \gamma Z \otimes Z)]$ each depend on three real parameters. That is, any information encoded into two qubits can be represented using Eq. 6 with the help of 15 parameters. For this work, we consider the simplest $\text{SU}(2)$ unitary for all four of the operators A_i , the identity operation, which reduces Eq. 7 to

$$U = N(\alpha, \beta, \gamma) \quad (7)$$

and the number of parameters to 3.

The circuit for implementing $N(\alpha, \beta, \gamma)$ is shown in Fig. 3 [28]. Each of the C and P unitaries in our work takes this form of some unitary $U \in \text{U}(4)$ and for each we chose an arbitrary set of three parameters (α, β, γ) . The circuits for our unitaries with these chosen parameters are shown in the Figs. 1 (b) and 1(c), respectively; alternate choices for these unitaries will also offer the same advantages in scaling with quantum resources that we subsequently discuss. That such a fiducial choice was successful showcases the tolerance of this kernel to choices of its hyperparameters.

Recall that encoding a data point with F features using the ZZFeatureMap requires on the order of F qubits and F^2 CNOT (entangling) gates. For the CPMMap, each U_1 and U_2 unitary requires 3 CNOT gates and focusing the data from n to $n/2$ qubits requires n C unitaries and $n/2$ U unitaries. The CPMMap thus only requires $\approx 9n$

entangling gates and, since it can encode F features on $n \approx F/2$ qubits, it only requires only $\approx 9F/2$ entangling gates to encode F features. Similarly, choosing a different focusing fraction m leads to even greater advantages. This improved scaling of the number of CNOT gates versus number of data features is the second reason that the CPMMap is more amenable to NISQ-era quantum devices than the ZZFeatureMap. The exact values of these comparisons are depicted in Fig. 2 where the advantages of the CPMMap are visually evident.

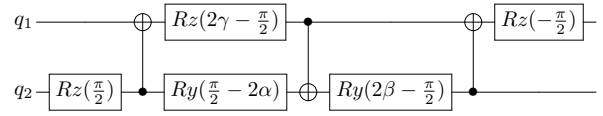


FIG. 3. A circuit for implementing the three-parameter two-qubit gate $N(\alpha, \beta, \gamma)$, requiring three CNOT gates.

B. Numerical Results

The performance of the CPMMap was benchmarked against several established quantum and classical kernels to ascertain its capabilities. We use several datasets characterized in Table I to check its performance as an SVC for classifying data into discrete categories.

Owing to the skewed nature of the majority of our test data, we opted for the Matthews Correlation Coefficient (MCC) as our primary evaluation criterion. For an in-depth explanation, kindly refer to Methods and Appendix A. MCC serves as a reliable metric, offer-

Dataset	Number of Features	Number of Instances	Classes
Ionosphere	34	351	2
Breast cancer Diagnostic (Wisconsin)	30	569	2
Credit card Fraud detection (Balanced)	30	984	2
Parkinson's disease (PD)	22	195	2
Stellar Classification Dataset - SDSS17	17	100000*	3*
Heart Disease	11	918	2
Titanic	10	891	2
Agaricus Lepiota Mushrooms	21	8145	2

TABLE I. Properties of various datasets used in this study. *The Stellar Classification Dataset properly has three classes, but we used only two of them, Galaxy and Star, combining for a total of 81039 data points.

ing a comprehensive assessment of binary classification outcomes by considering both true and false positives as well as negatives. A score of +1 in MCC denotes perfect prediction accuracy, 0 suggests no better than a random prediction, and -1 signifies a complete mismatch between the predicted and actual outcomes. It overcomes metrics such as accuracy that can give misleadingly positive results when classifiers are tested on skewed data.

In our research, we extensively utilized Qiskit's Statevector simulator, a tool designed to simulate the ideal quantum states of a quantum system without any external noise or decoherence. This simulator provides a precise representation of the quantum state, allowing for accurate computations and predictions. It is particularly beneficial for theoretical explorations and understanding the ideal behaviour of quantum algorithms. Alongside the Statevector simulator, we also employed Qiskit's noisy simulators. These are designed to mimic real IBM quantum devices by leveraging system snapshots. Such snapshots capture vital data about the quantum setup, including the coupling map, foundational gates, and qubit attributes (T1, T2, error rates, and more), proving instrumental for transpiler testing and conducting system simulations with noise. These noisy simulators present a more grounded view of quantum operations in tangible settings. Their use enabled us to assess the durability of our algorithms in authentic environments and refine them to better withstand quantum disruptions and other unforeseen challenges. We then proceeded to run small trials on `ibm_quebec` and `ibm_torino`.

1. Results with Seven Features After PCA

In the initial phase of our study, we employed principal component analysis (PCA) to reduce the feature

set size to seven across all datasets. Specifically, we limited the sample size of the Stellar Classification Dataset to 2,000 and excluded the QSO class to expedite the simulation process. For support vector classification, we leveraged the capabilities of both the SciKit Learn [29] and QisKit [21] libraries.

Our findings, in Fig. 4, reveal that the CPMMap consistently outshines the ZZFeatureMap quantum kernel across a diverse range of datasets. Remarkably, there were instances where the CPMMap not only matched but exceeded the performance of standard classical kernels [linear, polynomial (poly), radial basis function (RBF), sigmoid], highlighting its promising applications in the realm of quantum machine learning. The accompanying plots, which display Matthews Correlation Coefficient MCC scores, further substantiate the superior efficacy of the CPMMap. While some classical kernels exhibited strong performance on specific datasets, they faltered on others. In contrast, the CPMMap consistently delivered robust results, often rivaling or surpassing the best-performing classical kernels.

For some datasets, we repeated the CPMMap up to two times but uploaded the same features for each repetition. This increases the total number of CNOT gates by a factor of two but maintains the total number of qubits and the significant reduction in the number of CNOT gates; see Appendix C 1 for details.

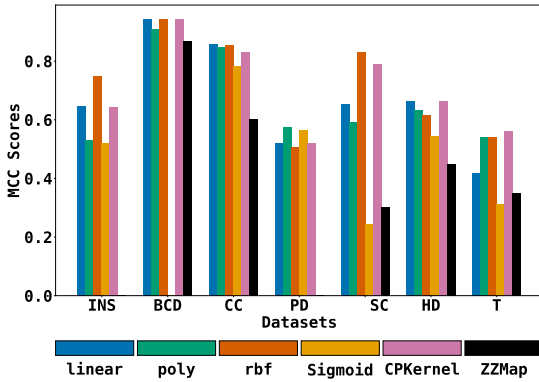


FIG. 4. MCC-score-based analysis of different kernels on different datasets scaled to each have 7 features, comparing the effectiveness of each kernel in handling specific types of data. The CPMap (second from right for each dataset) always outperforms the ZZFeatureMap (rightmost for each dataset) and always performs better than one or more of the classical kernels. For some datasets, certain kernels completely failed, so there is no bar visible for the ZZFeatureMap for the INS and PD datasets and for the sigmoid kernel for the BCD dataset. Dataset acronyms: Ionosphere (INS), Breast Cancer Diagnostic (BCD), Credit Card Fraud (CC), Parkinson’s Disease (PD), Stellar Classification (SC), Heart Disease (HD), and Titanic Survival (T).

2. Results for the Noisy Simulation with Seven Features

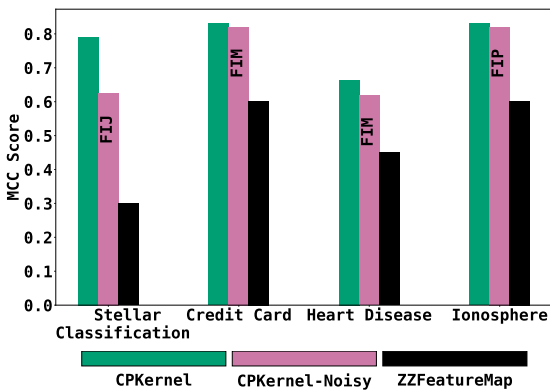


FIG. 5. MCC score for the noisy simulation of CPMap on different datasets. Here we used ‘fake_ibmq_jakarta’ (FIJ), ‘fake_ibmq_manila’ (FIM) and ‘fake_ibmq_perth’ (FIP) backends.

In addition to standard simulations, we conducted noisy simulations on three specific datasets: Stellar Classification, Balanced Credit Card, and Heart Disease. As demonstrated in Figure 5, our CPMap consistently surpassed the *noiseless* performance of ZZFeatureMap, even in the presence of noise.

3. A case for quantum advantage

Next, we turn to datasets with so many features that it is prohibitive to simulate the ZZFeatureMap on a classical computer due to the exorbitant qubit and gate-count requirements. We perform PCA on the Ionosphere dataset to reduce it to 22 features, in order to analyze it with the exact same CPMap as for the Parkinson’s dataset that has exactly 22 features.

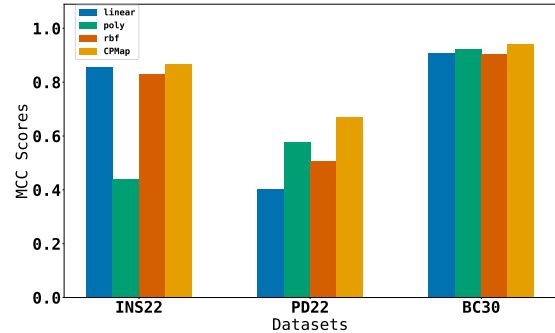


FIG. 6. This bar chart illustrates the MCC scores achieved by four kernel functions—from left to right: linear, polynomial (poly), radial basis function (RBF), and the CPMap—when applied to three different datasets.

The bar chart presented in Fig. 6 illustrates the performance of various kernels, including linear, poly, RBF, and CPMap, across the three distinct datasets: Ionosphere (INS22), Parkinson’s Disease (PD22), and Breast Cancer (BC30). Notably, the CPMap outperforms its counterparts across all datasets, achieving the highest MCC scores, indicative of its superior predictive capabilities. On the PD22 dataset, CPMap’s score is a significant leap from poly’s score and is even greater compared to the linear and RBF kernels. This trend persists with the INS22 and BC30 datasets, where CPMap consistently maintains the lead. Similar results are presented in Appendix D with even more features per dataset and results for different numbers of repetitions of the CPMap in Appendix C2.

The consistent outperformance by CPMap across diverse datasets suggests a promising avenue for achieving quantum advantage in predictive tasks. The substantial margin by which CPMap leads for datasets with large numbers of features hints at its unique ability to capture complex patterns that classical kernels might not discern as effectively, thereby bolstering the hypothesis that quantum machine learning could offer computational benefits over traditional algorithms.

C. Statistical Significance Testing

In addition to demonstrating quantum advantage, we further validated the performance of our custom CPMap kernel against traditional RBF, poly, and linear kernels using Parkinson's disease dataset. We employed statistical significance testing to confirm the superiority of CPMap in terms of accuracy and the MCC.

We performed paired t-tests to evaluate the significance of performance differences between the CPMap kernel and the traditional kernels (RBF, Poly, and Linear) in terms of accuracy and MCC scores across 80 independent runs. The results are summarized in Table II.

TABLE II. Paired t-Test Results Comparing CPMap with Other Kernels

Comparison	Metric	t-Statistic	p-Value
RBF vs. CPMap	Accuracy	8.45	1.15×10^{-12}
RBF vs. CPMap	MCC	8.54	7.83×10^{-13}
POLY vs. CPMap	Accuracy	11.38	2.57×10^{-18}
POLY vs. CPMap	MCC	11.32	3.28×10^{-18}
Linear vs. CPMap	Accuracy	11.60	9.78×10^{-19}
Linear vs. CPMap	MCC	11.26	4.26×10^{-18}

The t-statistics and p-values indicate that the performance differences between the CPMap kernel and each of the traditional kernels are statistically significant. The t-statistics exceed typical critical values, and the p-values are significantly below standard significance levels (e.g., 0.05, 0.01), thereby rejecting the null hypothesis of no difference in performance.

Performance Metrics Summary: To provide a detailed view of the CPMap kernel's performance, we calculated the mean and standard deviation of accuracy and MCC scores across the 80 runs for each kernel. These metrics are detailed in Table III.

Figures 7 and 8 illustrate the distribution of accuracy

TABLE III. Mean and Standard Deviation of Accuracy and MCC for Different Kernels

Kernel	Accuracy		MCC	
	Mean	Std	Mean	Std
Linear	0.8615	0.0442	0.6102	0.1333
Poly	0.8660	0.0424	0.6135	0.1354
CPMap	0.9234	0.0388	0.7898	0.1118
RBF	0.8785	0.0477	0.6532	0.1438

and MCC scores across the different kernels. These visualizations highlight the consistent superior performance of the CPMap kernel.

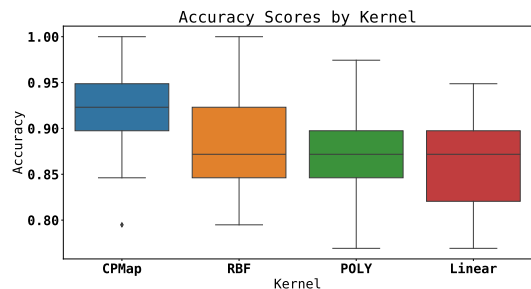


FIG. 7. Box Plot of Accuracy Scores for Different Kernels

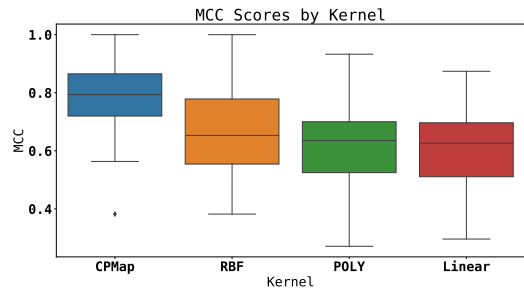


FIG. 8. Box Plot of MCC Scores for Different Kernels

This statistical analysis and visualization confirm the significant advantage of the CPMap kernel over traditional kernels in the context of Parkinson's disease data, reinforcing the potential for quantum machine learning to achieve computational superiority in predictive tasks.

D. Test on IBM's Hardware

To investigate the feasibility and performance of

our CPMMap quantum kernel on real superconducting quantum processors, we conducted experiments on two IBM devices: the 127-qubit `ibm_quebec` (Eagle-class) and the 133-qubit `ibm_torino` (Heron-class). All experiments targeted a binary classification task using the Parkinson’s disease dataset, which originally contains 195 samples and 22 numerical features per instance. The qubit configurations, data preprocessing, and mitigation strategies can be found in the Methods section.

1. Test with full dataset on `ibm_quebec`

We evaluated the CPMMap kernel on IBM’s 127-qubit `ibm_quebec` device using the full 22-feature Parkinson dataset encoded on 12 qubits. To assess kernel performance, we ran tests across three transpiler optimization levels and applied error mitigation techniques including dynamical decoupling (DD), zero noise extrapolation (ZNE), and probabilistic error cancellation (PEC). In all cases, the average entropy of the output was approximately same as the number of qubits, which implies the outputs yielded no meaningful information. Specifically, entropy values ranged from 11.58 to 11.66 across all runs—very close to the maximum possible for a 12-qubit system. This was attributed both to CPMMap’s requirement for all-to-all connectivity—which introduces numerous SWAP operations and deepens the circuit—and to the high noise levels inherent to the `ibm_quebec` device.

We also performed a small test on the newer 133-qubit `ibm_torino` (Heron-class) device using a subset of the Parkinson dataset. In contrast to `ibm_quebec`, the output entropy on `ibm_torino` remained within a reasonable range, with values ranging from 5.59 to 9.79—well below the 12-qubit maximum—indicating that the circuits retained meaningful structure. This suggests that the full dataset could feasibly be processed on this hardware. However, due to limited device access, we conducted the experiment with 7 PCA-reduced features mapped to 4 qubits. The classification results are reported below.

2. Test with PCA-reduced dataset on `ibm_quebec`

We tested the CPMMap kernel on IBM’s `ibm_quebec` device using 4 qubits (7 input features) and no error mitigation for Parkinson’s disease classification. Experiments were performed on qubit chains 39-40-41-42 or 39-40-41-53. The calibration data for these qubits

indicate the following average values: 3.39×10^{-3} s for T1, 2.37×10^{-3} s for T2, and 3.82×10^{-3} for the two-qubit gate error rate. In this trial, we obtained an MCC score of 0.34 and an accuracy comparable to simulation (see Fig 9). While the result is still affected by hardware noise, it marks the first instance where this kernel produced a meaningful result on real hardware.

As mentioned above, one limiting factor is the device’s restricted qubit connectivity, which requires the transpiler to insert multiple SWAP gates during compilation, increasing the number of CNOT operations and overall circuit depth. This opens the path to explore optimal compilation of our kernel in architectures with limited connectivity and realization in platforms such as trapped ions where qubit connectivity is not constrained.

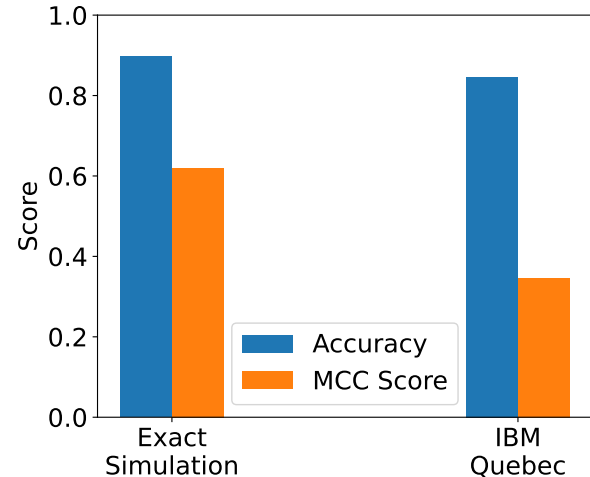


FIG. 9. Performance comparison of the CPMMap kernel for Parkinson’s disease classification. Accuracy and MCC Score are shown for both exact simulation and IBM’s `ibm_quebec` (4-qubit encoding).

3. Test with PCA reduced dataset on `ibm_torino`

In this case, we deployed our CPMMap kernel circuit on IBM’s `ibm_torino`, a 133-qubit superconducting quantum processor belonging to the Heron family. Heron-class devices feature improvements in qubit coherence and native two-qubit gate implementations. According to IBM Quantum’s platform, this device has a T1 time of 1.83×10^{-4} s and T2 time of 1.41×10^{-4} s.

The quantum kernel matrix was computed in a single run across the full dataset and training and test matrices were extracted without recomputation. We allocated 80 samples for training and 20 for testing.

Despite inevitable hardware noise, the quantum kernel executed on `ibm_torino` demonstrated strong performance. It achieved an MCC of 0.68 and an accuracy of 0.85 (see Fig. 10). Among the three kernels evaluated, the simulated CPMMap kernel achieved the highest performance (MCC of 0.90, accuracy of 0.95), followed by the classically optimized RBF kernel (MCC of 0.78, accuracy of 0.90), and finally, the CPMMap executed on real hardware. Notably, the ZZFeatureMap kernel, simulated under *ideal noiseless* conditions, yielded an MCC of 0.00, failing to capture any useful structure in this task. This further underscores the practical relevance of our CPMMap.

The observed performance gap between the statevector simulation and the real-device execution can be attributed to decoherence, gate errors, and limited circuit depth. Nevertheless, the successful deployment of CPMMap on `ibm_torino` confirms its feasibility on today's NISQ devices and underscores the promise of quantum kernels in practical machine learning tasks.

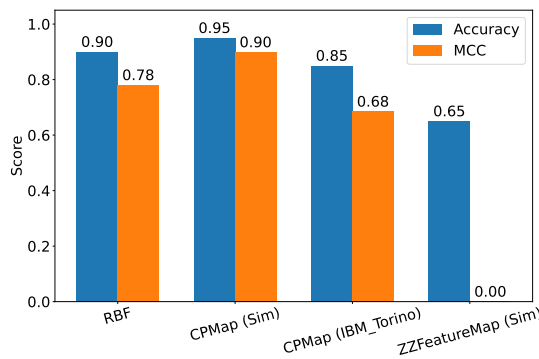


FIG. 10. Comparison of CPMMap based kernel on the curated Parkinson dataset. The simulated CPMMap-based Kernel achieves the highest performance, followed by RBF and quantum hardware (`ibm_torino`).

III. DISCUSSION AND CONCLUSION

Our proposed feature map paves the way for the application of quantum machine learning algorithms to more complex and higher-dimensional data, even

with limited qubit resources. The CPMMap's remarkable efficiency in qubit utilization, evident through its requirement of approximately $\frac{N}{2}$ qubits to represent N features, marks a substantial improvement over the ZZFeatureMap. This efficiency not only eases the computational load but also enhances the scalability of quantum models. In our comparative analysis with classical kernels such as the RBF, linear, and polynomial kernels, the CPMMap sometimes demonstrated superior performance. Our finding demonstrate the potential for quantum algorithms to outperform their classical counterparts under specific conditions, especially when dealing with high-dimensional data and limited training samples.

The operational feasibility of the CPMMap is another cornerstone of our research. Its reduced circuit depth, as opposed to the computationally intensive ZZFeatureMap, enabled us to successfully simulate complex datasets, due to the significant reduction in number of entangling gates required for our scheme. This aspect of the CPMMap not only addresses the current limitations in quantum computing resources but also makes quantum machine learning models more accessible and practical for a broader range of applications.

The implications of our findings extend beyond the immediate scope of this study. The CPMMap's promising performance in efficiently handling high-dimensional datasets opens new pathways for future work, particularly in applying quantum algorithms to more complex and diverse datasets with applications in health sciences to material discovery. Further exploration into its realization existing noisy quantum computing platforms and future small scale fault-tolerant devices, as opposed to simulations, could offer deeper insights into its practical utility and performance in real-world applications.

Our proposed CPMMap is expected to replace the existing Pauli feature maps due its significantly improved performance at reduced resource requirements in terms of the number of qubits and CNOT gates with respect to the number of features. This goes beyond a theoretical promise through our numerical demonstrations and small-scale implementation on a noisy quantum computer. We expect the CPMMap protocol to play a crucial role in advancement of quantum machine learning and in developing its early applications on realistic problems with performance that can potentially beat existing classical methods.

IV. METHODS

In this study, we introduce an instance of the CPMMap, specifically designed for data classification using the kernel method across various standard datasets. The CPMMap simulation is conducted utilizing two distinct environments: Qiskit’s Statevector simulator and its Noisy counterpart, providing a comprehensive analysis of its performance under varied conditions. The datasets employed in this investigation are sourced from standard online repositories, namely Kaggle and the UCI dataset library, ensuring a diverse and robust set of data for evaluation. To facilitate the support vector classification process, we employ the built-in SVC function from Scikit-learn, a widely recognized tool in machine learning. This section details the parameters, methodologies, and evaluation techniques utilized in the development and assessment of the CPMMap, aiming to demonstrate its effectiveness and versatility in data classification tasks.

To address the limitations of conventional metrics on imbalanced datasets (see Appendix A), the MCC was employed. MCC is a balanced metric that takes into account both over-predictions and under-predictions across classes. It is defined as

$$\text{MCC} = \frac{TP \times TN - FP \times FN}{\sqrt{(TP+FP)(TP+FN)(TN+FP)(TN+FN)}}, \quad (8)$$

where TP, TN, FP, and FN are the numbers of true positives, true negatives, false positives, and false negatives, respectively. The MCC returns a value in $(-1, 1)$, with 1 representing perfect prediction, -1 indicating total disagreement between prediction and observation, and 0 suggesting no better than random prediction. MCC is particularly valuable for imbalanced datasets as it considers all four components of the confusion matrix and is less susceptible to the bias of a large class [30].

To facilitate a comprehensive comparison, we utilized seven distinct features for each dataset when evaluating the CPMMap against the ZZFeatureMap. This choice is strategically made, considering that the ZZFeatureMap demands one qubit per feature and, notably, the number of CNOT gates required for the ZZFeatureMap increases quadratically with the number of features. Such rapid growth renders the simulation of larger datasets challenging. Opting for seven features strikes a balance, allowing for a meaningful comparison while keeping the computational requirements within manageable limits. In contrast to the ZZFeatureMap, the CPMMap demonstrates remark-

able efficiency in qubit utilization, requiring a mere four qubits to represent these seven features—a notable advancement over the ZZFeatureMap kernel. Moreover, we have benchmarked the CPMMap’s performance against several classical kernels, namely the RBF, linear, and polynomial kernels, to establish a baseline comparison.

For the noisy simulation, we targeted three distinct datasets: Stellar Classification, Balanced Credit Card, and Heart Disease. To accommodate computational limitations and manage extended runtimes, we applied PCA to reduce the dimensionality of the Heart Disease and Balanced Credit Card datasets, ultimately selecting the seven most informative features for these simulations. These noisy simulations were conducted using Qiskit’s advanced noisy simulators, designed to mimic the behaviour of actual quantum computers, thereby providing a more realistic assessment of our models’ performance in quantum computing environments. For the Balanced Credit Card and Heart Disease datasets, we utilized the **fake_ibmq_manila** backend, a simulator that emulates the noise characteristics of the IBMQ Manila quantum device. To avoid cherry picking, for the Stellar Classification dataset, we employed the **fake_ibmq_jakarta** backend, replicating the conditions of the IBMQ Jakarta, and for the Ionosphere dataset, we used **fake_ibm_perth**. These choices allowed us to assess the robustness of our models against realistic quantum noise and error rates. The results from these simulations, highlighting the impact of quantum noise on model accuracy and reliability, are detailed in Fig. 5, providing critical insights into the potential real-world performance of quantum machine learning algorithms.

In our experiments, we also processed the datasets in their entirety using the CPMMap without resorting to Principal Component Analysis (PCA) for dimensionality reduction. This approach provides a more authentic test of the CPMMap’s capability to handle high-dimensional data. Specifically, in the case of the Breast Cancer dataset, which requires sixteen qubits to represent thirty features, we observed that the CPMMap necessitates significantly less circuit depth. This efficiency advantage enabled us to successfully simulate the model on a personal computer without encountering computational bottlenecks. It is crucial to note that running the Breast Cancer dataset with all 30 features using the ZZFeature Map was not feasible due to its computational expensiveness and the near impossibility of simulating 30 qubits with such high depth on personal computers. Notably, the quantum Kernel based on CPMMap exhibited superior performance compared

to the classical kernels in analyzing the Breast Cancer, Heart Disease datasets, thereby demonstrating its potential for practical applications in quantum machine learning and indicating a promising direction for further research in this area.

We conducted experiments on IBM’s superconducting quantum processors. Specifically, we tested our circuits on two real devices: `ibm_quebec` (127-qubit Eagle-class) and `ibm_torino` (133-qubit Heron-class). These evaluations were performed on the Parkinson’s disease dataset. On `ibm_quebec`, we used all 22 features mapped to 12 qubits, as well as a PCA-reduced 7-feature input encoded on 4 qubits. For the 12 qubit case, error mitigation techniques including dynamical decoupling, zero noise extrapolation, and probabilistic error cancellation were applied in combination with varying transpilation levels to analyze hardware-induced deviations. On `ibm_torino`, we performed an end-to-end kernel classification task using a curated subset of 100 samples selected via classical SVM pre-filtering, ensuring a mix of easy and ambiguous cases. We did not use any error mitigation technique for this task. The quantum kernel matrix was constructed in a single batch run, and training/testing splits were extracted without recomputation. These experiments allowed us to benchmark our kernel’s performance un-

der real-device noise and confirm its competitiveness with classically optimized models, demonstrating the CPMap’s potential viability on current NISQ hardware.

V. ACKNOWLEDGMENTS

The authors would like to acknowledge the use of IBM Quantum services for this work and in particular the Qiskit package [21], as well as fruitful discussions with Anaelle Hertz and Barry Sanders. We thank Marco Armenta for assisting with the execution of our experiments on the IBM Quebec quantum device. AZG and KH acknowledge that the NRC headquarters is located on the traditional unceded territory of the Algonquin Anishinaabe and Mohawk people. K.H. acknowledges funding from the NSERC Discovery Grant and Alliance programs.

VI. DATA AVAILABILITY

Data and code related to this research can be found at this private [GitHub repository](#) upon reasonable request.

[1] L. Chen, in *Encyclopedia of Database Systems* (Springer, Boston, MA, Boston, MA, USA, 2009) pp. 545–546.

[2] V. Berisha, C. Krantsevich, P. R. Hahn, S. Hahn, G. Dasarathy, P. Turaga, and J. Liss, *npj Digital Med.* **4**, 1 (2021).

[3] A. A. Awan, [DataCamp](#) (2023).

[4] V. Havlíček, A. D. Córcoles, K. Temme, A. W. Harrow, A. Kandala, J. M. Chow, and J. M. Gambetta, *Nature* **567**, 209 (2019).

[5] E. Peters, J. Caldeira, A. Ho, S. Leichenauer, M. Mohseni, H. Neven, P. Spentzouris, D. Strain, and G. N. Perdue, *npj Quantum Inf.* **7**, 1 (2021).

[6] T. Kusumoto, K. Mitarai, K. Fujii, M. Kitagawa, and M. Negoro, *npj Quantum Inf.* **7**, 1 (2021).

[7] S. L. Wu, S. Sun, W. Guan, C. Zhou, J. Chan, C. L. Cheng, T. Pham, Y. Qian, A. Z. Wang, R. Zhang, M. Livny, J. Glick, P. Kl. Barkoutsos, S. Woerner, I. Tavernelli, F. Carminati, A. Di Meglio, A. C. Y. Li, J. Lykken, P. Spentzouris, S. Y.-C. Chen, S. Yoo, and T.-C. Wei, *Phys. Rev. Res.* **3**, 033221 (2021).

[8] D. Alaminos, M. B. Salas, and M. A. Fernández-Gámez, *Comput. Econ.* **59**, 803 (2022).

[9] S. Lloyd, M. Mohseni, and P. Rebentrost, *Nat. Phys.* **10**, 631 (2014).

[10] J. Biamonte, P. Wittek, N. Pancotti, P. Rebentrost, N. Wiebe, and S. Lloyd, *Nature* **549**, 195 (2017).

[11] M. Schuld, I. Sinayskiy, and F. Petruccione, *Contemp. Phys.* **56**, 172 (2015).

[12] M. Schuld and N. Killoran, *Phys. Rev. Lett.* **122**, 040504 (2019).

[13] M. Schuld, arXiv [10.48550/arXiv.2101.11020](https://arxiv.org/abs/10.48550/arXiv.2101.11020) (2021), [2101.11020](#).

[14] A. Asfaw, L. Bello, Y. Ben-Haim, S. Bravyi, L. Capelluto, A. C. Vazquez, J. Ceroni, R. Chen, A. Frisch, J. Gambetta, S. Garion, L. Gil, S. D. L. P. Gonzalez, F. Harkins, T. Imamichi, D. McKay, A. Mezzacapo, Z. Minev, R. Movassagh, G. Nannicini, P. Nation, A. Phan, M. Pistoia, A. Rattew, J. Schaefer, J. Shabani, J. Smolin, K. Temme, M. Tod, and S. Wood, *Learn Quantum Computation Using Qiskit* (2020).

[15] I. Cong, S. Choi, and M. D. Lukin, *Nat. Phys.* **15**, 1273 (2019).

[16] C. Zoufal, A. Lucchi, and S. Woerner, *npj Quantum Inf.* **5**, 1 (2019).

[17] A. Pérez-Salinas, A. Cervera-Lierta, E. Gil-Fuster, and J. I. Latorre, *Quantum* **4**, 226 (2020).

- [18] B. Roy, All about data encoding for quantum machine learning.
- [19] J. Preskill, *Quantum* **2**, 79 (2018), 1801.00862v3.
- [20] T. Hubregtsen, J. Pichlmeier, P. Stecher, and K. Bertels, *Quantum Mach. Intell.* **3**, 9 (2021).
- [21] Qiskit contributors, Qiskit: An open-source framework for quantum computing (2023).
- [22] X. Vasques, H. Paik, and L. Cif, *Sci. Rep.* **13**, 1 (2023).
- [23] H.-J. Kim, G.-J. Song, K.-B. Jang, and H.-J. Seo, in *2021 IEEE International Conference on Consumer Electronics-Asia (ICCE-Asia)* (IEEE) pp. 01–03.
- [24] A. Abbas, D. Sutter, C. Zoufal, A. Lucchi, A. Figalli, and S. Woerner, *Nat. Comput. Sci.* **1**, 403 (2021).
- [25] D. T. Mukhamedieva, *E3S Web Conf.* **494**, 04026 (2024).
- [26] View of Meta-Fibonacci Sequences, Binary Trees and Extremal Compact Codes (2024), [Online; accessed 22. Jan. 2024].
- [27] 1,2,2,3, 4, 4, 4, 5, 6, 6, 7, 8, 8, 8, 8, 9, 10, 10, 11, 12, 12, 12, 13, 14, 14, 15, 16, 16, 16, 16, 16, 17 - OEIS (2024), [Online; accessed 22. Jan. 2024].
- [28] F. Vatan and C. Williams, *Phys. Rev. A* **69**, 032315 (2004).
- [29] F. Pedregosa, G. Varoquaux, A. Gramfort, V. Michel, B. Thirion, O. Grisel, M. Blondel, P. Prettenhofer, R. Weiss, V. Dubourg, J. Vanderplas, A. Passos, D. Cournapeau, M. Brucher, M. Perrot, and E. Duchesnay, *Journal of Machine Learning Research* **12**, 2825 (2011).
- [30] D. Chicco, *BioData Mining* **10**, 1 (2017).
- [31] T. Fawcett, *Pattern Recognit. Lett.* **27**, 861 (2006).
- [32] D. Chicco and G. Jurman, *BMC Genomics* **21**, 1 (2020).
- [33] N. Japkowicz and S. Stephen, *Intell. Data Anal.* **6**, 429 (2002).
- [34] L. A. Jeni, J. F. Cohn, and F. De La Torre, in *2013 Humanine Association Conference on Affective Computing and Intelligent Interaction* (IEEE, 2013) pp. 245–251.
- [35] M. Sokolova and G. Lapalme, *Information Processing & Management* **45**, 427 (2009).

Appendix A: On the Suitability of Regular Machine Learning Metrics

In the realm of machine learning, the evaluation of model performance is paramount. Common metrics such as accuracy, precision, recall, and F1 score are frequently employed to gauge the efficacy of models. However, these metrics, while widely accepted, are not universally applicable across all scenarios.

Imbalanced datasets, where one class significantly outnumbers the other, present a unique challenge for machine learning models and the evaluation metrics used to assess their performance. This is particularly true for binary classification tasks, where the minority class is often of greater interest than the majority class.

1. Limitations of Conventional Metrics

Traditional performance metrics, such as accuracy, can be misleading in the context of imbalanced datasets [31]. Consider a dataset with 95% samples of class A and only 5% samples of class B. A naive classifier predicting all samples as class A will still achieve a superficially high accuracy of 95%. This demonstrates that accuracy alone is not sufficient to evaluate model performance on imbalanced datasets [32, 33].

Similarly, other metrics such as recall, precision, and the F1 score can sometimes provide a skewed perspective when classes are imbalanced. There are situations where models can achieve high values for these metrics by being biased towards the majority class, rendering them less effective as measures of model performance [34, 35]. This is why we employ the Matthews Correlation Coefficient (MCC), as described in the Methods section.

2. Numerical Comparison:

The bar plot (Fig. 11) comparing the accuracy and MCC scores across the three datasets Ionosphere, Parkinson’s Disease, and Stellar Classification illustrates why the MCC score can be a more informative metric than accuracy, particularly in specific contexts such as imbalanced datasets or when true negatives are significant.

Firstly, in the Stellar Classification dataset, while the accuracy is relatively high (0.7225), the MCC score is notably lower (0.3003). This disparity suggests that although the model has a high rate of correct predictions (accuracy), its ability to balance true and false positives and negatives is less proficient, as captured by the MCC score. MCC takes into account all four categories of the confusion matrix (true positives, false positives, true negatives, and false negatives), offering a more balanced measure of the quality of binary classifications, especially in cases where class distribution is uneven.

Secondly, for the other two datasets, the MCC scores are zero despite the accuracies being 0.6056 and 0.7458, respectively. This indicates a situation where the model might be making correct predictions by chance or through bias towards the majority class, a common issue in imbalanced datasets. In such scenarios, accuracy alone can be misleading, as it does not distinguish between the types of errors made by the model. MCC, on the other hand, by being sensitive to the balance among all four confusion matrix categories, gives a more faithful representation of the model’s performance.

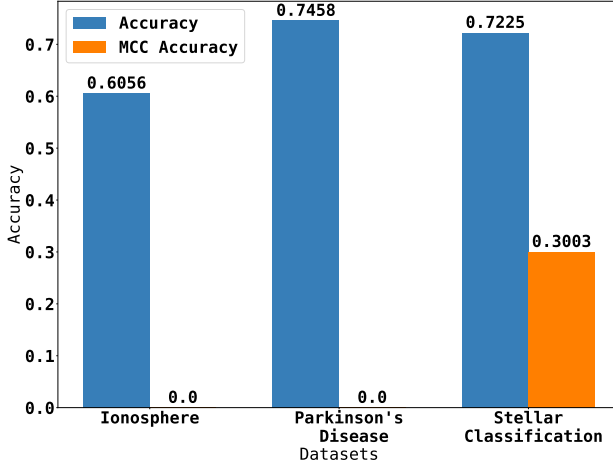


FIG. 11. Evaluating accuracy (left bar, blue) vs. MCC (right bar, orange) across Ionosphere, Parkinson's Disease, and Stellar Classification datasets. Note that the MCC bar vanishes for the left two datasets.

3. Conclusion

When assessing machine learning models on datasets with imbalances, exclusive dependence on conventional metrics can result in skewed insights. The MCC presents a more encompassing and impartial assessment criterion, aptly fitting for tasks with class disparities. It is pivotal to select a performance measure that resonates with the distinct demands and traits of the problem at hand. Particularly in quantum machine learning, given the distinct nature of data and the nuances of the models, a mere reliance on metrics established for tasks other than the one at hand may fall short in truly capturing the model's efficacy.

Appendix B: ZFeatureMap vs. ZZFeatureMap

The ZFeatureMap is a simple feature map that involves rotations around the z axis of the Bloch sphere. On the other hand, the ZZFeatureMap is made from two-qubit gates that involve both rotations around the z axis and controlled-X (CNOT) gates. This makes the ZZFeatureMap more expressive and capable of capturing more complex relationships in the data.

The primary reason for preferring the ZZFeatureMap over the ZFeatureMap in quantum machine learning is the former's ability to generate entanglement between qubits. Entanglement is a uniquely quantum phenomenon and is believed to be one of the reasons quantum algorithms can outperform classical ones [4, 14]. By using the ZZFeatureMap, quantum machine learning algorithms can leverage this entanglement to potentially achieve better performance.

While both the ZFeatureMap and ZZFeatureMap have their applications, the latter is generally preferred in quantum machine learning due to its ability to capture more complex data relationships and leverage quantum entanglement.

Appendix C: Repeating the kernel to reupload the same data

1. Seven features

In Table IV, we present the efficacy of two quantum machine learning kernels, CPMMap and ZZFeatureMap, across a variety of datasets, evaluated using the Matthews Correlation Coefficient (MCC). Each dataset was reduced to seven principal components, except for the Titanic dataset, where PCA was not applied, as indicated by an asterisk. The MCC scores serve as a quantitative measure of model performance, with a score of zero indicating no learning.

Regarding the number of repetitions (NOR), CPMMap consistently outperformed ZZFeatureMap, even when only a single repetition was used. Specifically, the MCC scores for ZZFeatureMap dropped to zero for some datasets, suggesting no learning occurred, a situation not observed with CPMMap. For ZZFeatureMap, the optimum performance was achieved with a single repetition, while additional repetitions led to a decrease in MCC scores, contrary to expectations. In contrast, CPMMap's performance was enhanced with repetitions, as demonstrated by higher MCC scores across several datasets. This pattern also underscores the variable impact of the number of repetitions on different algorithms and the importance of tailored approaches in model training.

Dataset	NOF Used	NOR for CPMMap	NOR for ZZFeatureMap	MCC Score CPMMap	MCC Score ZZFeatureMap	MCC Score CPMMap with 1 Reps
Ionosphere	7	1	1	0.643	0.0	0.643
Breast cancer Diagnostic	7	2	1	0.944	0.869	0.926
Credit card (Balanced)	7	1	1	0.831	0.602	0.831
Parkinson's disease (PD)	7	2	1	0.520	0.0	0.451
Stellar Classification	7	2	1	0.791	0.300	0.778
Heart Disease	7	2	1	0.664	0.449	0.621
Titanic	7*	1	1	0.561	0.351	0.561

TABLE IV. Data and model characteristics for datasets with seven features. NOF: Number of features; NOR: Number of repetitions; *without PCA.

2. All features

In Table V, we present the efficacy of the CPMMap in learning tasks across six datasets, emphasizing the model's robustness without substantial feature reduction, each with varying requirements for quantum resources, especially the number of repetitions of the CPMMap circuits. The datasets under consideration included Ionosphere, Breast Cancer Diagnostic, Credit Card (Balanced), Parkinson's Disease (PD), Stellar Classification, and Agaricus Lepiota Mushrooms. The number of features utilized ranged from 16 to 30, with an asterisk indicating datasets where Principal Component Analysis (PCA) was not employed. The quantum resource requirement, measured in qubits, was predominantly 12, except for Stellar Classification, which required 9. The assessment metric, MCC, was reported for multiple repetitions of the CPMMap and a singular repetition to investigate the impact of repetition on performance. Notably, the MCC scores exhibited a broad spectrum, with Parkinson's Disease recording the lowest at 0.672, while Agaricus Lepiota Mushrooms achieved an impressive high of 0.996. This variance underscores the model's performance sensitivity to the inherent characteristics of the dataset.

Appendix D: Results for higher number of features

This section presents findings using exclusively the CPMMap and a greater number of features, including the full set. In this comparison, the ZZFeatureMap was not utilized, as simulation attempts on our computers consistently resulted in memory errors. This suggests that employing ZZFeatureMap is computationally demanding.

Dataset	NOF Used	NOR for CPMap	Qubits Required	MCC Score	MCC Score with 1 repetition	Accuracy
Ionosphere	22	2	12	0.866	0.832	0.930
Breast cancer Diagnostic	30*	2	16	0.943	0.908	0.974
Credit card (Balanced)	22	5	12	0.950	0.942	0.934
Parkinson's disease (PD)	22*	1	12	0.672	0.672	0.881
Stellar Classification	16	3	9	0.956	0.946	0.982
Agaricus Lepiota Mushrooms	21*	6	12	0.996	0.910	0.998

TABLE V. Data and model characteristics for datasets with all features. NOF: Number of features; NOR: Number of repetitions; *without PCA.

Figure 12 presents a comparison of MCC scores for several datasets, with all the features, encompassing Parkinson's Disease with 22 features (PD22), Breast Cancer with 30 features (BC30), Agaricus Lepiota Mushroom with 21 features (ALM21), and Stellar Classification with 17 features (SC17). For the Stellar Classification dataset specifically, the analysis was focused on two classes, totaling 81,039 entries. The bar graph demonstrates that CPMap consistently achieves high MCC scores across these datasets, showcasing its capacity to effectively manage and interpret datasets with a substantial number of features. These results indicate that CPMap has the potential to surpass traditional kernel functions, affirming its suitability for complex, large-scale data analysis.

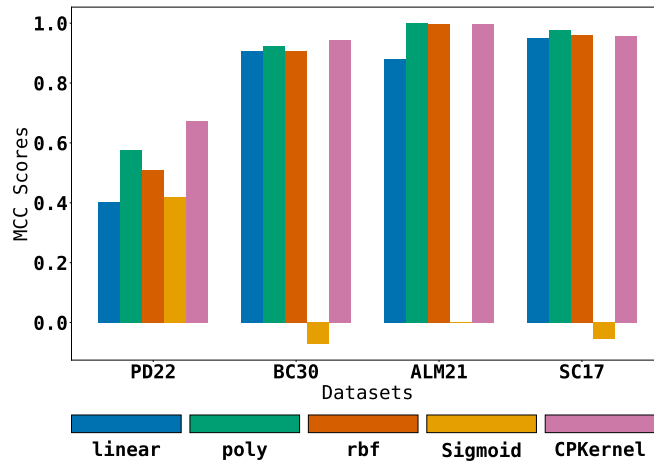


FIG. 12. Comparative Analysis of MCC Scores for various datasets with all the Features, including Parkinson's Disease with 22 features (PD22), Breast Cancer with 30 features (BC30), Agaricus Lepiota Mushroom with 21 features (ALM21) and Stellar Classification with 17 features (SC17).